PERGAMON

International Journal of Multiphase Flow 26 (2000) 17–44

International Journal of Multiphase Flow

www.elsevier.com/locate/ijmulflow

Influence of shear and elongation on drop deformation in convergent–divergent flows

Roger E. Khayat[a,*], A. Luciani[b], L.A. Utracki[c], F. Godbille[d], J. Picot[d]

[a]*Department of Mechanical and Materials Engineering, Faculty of Engineering Science, The University of Western Ontario, London, Ontario, Canada, N6A 5B9*

[b]*Ecole Polytechnique Federale de Lausanne, Laboratoire de Technologie des Composites et Polymeres, LTC-DMX-EPFL, 1015, Lausanne, Switzerland*

[c]*National Research Council of Canada, Industrial Materials Institute, 75 de Mortagne blvd, Boucherville, QC, Canada, J4B 6Y4*

[d]*Department of Chemical Engineering, The University of New Brunswick, Fredericton, N.B., Canada, E3B 5A3*

Received 13 March 1998; received in revised form 2 December 1998

Abstract

The effects of shear and elongation on drop deformation are examined through numerical simulation and experiment. A two-dimensional formulation within the scope of the boundary element method (BEM) is proposed for a drop moving under the influence of an ambient flow inside a channel of a general shape, with emphasis on a convergent–divergent channel. Both the drop and the suspending fluid can be either Newtonian or viscoelastic of the Maxwell type. The predicted planar deformation is found to provide accurate description of the physical reality. For example, small drops, flowing on the axis, elongate in the convergent part of the channel, then regain their circular form in the divergent part, confirming the experimental observations. Drops placed off-axis are found to rotate during the flow. These drops thus have longer residence time as well as larger and irreversible deformation than those moving on the axis. Both theory and experiment show a difference in deformability for Newtonian and viscoelastic drops in a slit flow. Initially, a Newtonian drop is reluctant to deform, but then deformation is rapid. A viscoelastic drop initially deforms readily, but then the deformation slows down. The slit flow does not flatten drops whose diameter is at least 10 times smaller than the slit gap. The effects of shear and elongation stress, the viscosity ratio, the drop diameter-to-channel-gap ratio, the initial drop position, the interfacial tension, and elasticity of the dispersed and ambient phases were examined using the BEM. © 1999 Elsevier Science Ltd. All rights reserved.

* Corresponding author. Tel.: +1-519-679-2111 (ext. 8253); fax: +1-519-661-3020.
E-mail address: khayat@engga.uwo.ca (R.E. Khayat).

0301-9322/00/$ - see front matter © 1999 Elsevier Science Ltd. All rights reserved.
PII: S0301-9322(98)00083-4

1. Introduction

This paper examines the interplay between shear and elongation during drop deformation in convergent–divergent channels, with reference to mixing. Preparation of polymer blends requires the mechanical mixing of at least two macromolecular species (and additives) for optimal morphology. Most blends are prepared in either a single- or a twin-screw extruder where the flow is dominated by shear. Mixing in the shear field is deficient. To generate the same deformation in shear flow, a greater amount of energy is required than in extensional flow (Erwin, 1991). More importantly, shear flow is incapable of dispersing liquids with viscosity four times that of the matrix liquid. The extensional flow field is more efficient for generating the dispersive as well as the distributive mixing (Grace, 1971).

Numerous authors have pointed to the great potential of the extensional flow for efficient mixing of immiscible liquids having large differences in rheological properties, particularly the drop-to-suspending fluid viscosity ratio, R_η, at constant stress. For example, flow of 30 wt% polyamide-6, PA-6, dispersed in high density polyethylene, HDPE, at $T = 150^\circ$C (that is 79°C *below* the melting point of PA-6) results in fibrillation of the PA-6 domains. The calculated extensional stresses at the entrance of the die, $\sigma_{11} = 50$–800 kPa, far exceeds the measured tensile yield stress at this temperature, $\sigma = 15$ kPa (Utracki et al., 1986). The theoretical and experimental works of Erwin (1991) on the laminar mixing demonstrated that: (i) the deformation of the dispersed phase at the same imposed strain (as measured by the generated interfacial area) is far greater in extension than it is in shear; (ii) the rate of spatial separation of two material points in extension is greater than that in shear by several orders of magnitude; and (iii) the energy required to generate the same increase of the interfacial area in extension is substantially lower than that required in shear (e.g. at current-to-initial interface ratio of 1000, the energy per unit volume consumed in extensional mixing is 6800 times smaller than in shear). Other studies, with Newtonian or non-Newtonian systems, confirmed these observations. For example, Han (1981) and his collaborators reported that the extensional flow breaks up drops passing through a convergence into mini-drops with diameters one order of magnitude smaller. Elmendorp's calculations demonstrated a great advantage of the 'stretching and folding' mechanism of mixing in extensional flow (Elmendorp, 1986).

During the last 20 years, several authors made use of extensional flow mixing for the polymeric systems. For example, Suzaka (1982) patented an extensional flow mixer, which was composed of a series of plates placed across the flow channel. A polymer blend was forced to pass through a series of convergences and divergences, which elongated the drops and then dispersed them. However, all orifices were of the same size, and the stresses decreased from the first plate to the next. As a result, the mixer provided good mixing for only some systems. Furthermore, the device could be optimized only by trial and error. Any change in the resin required the process to be interrupted, the mixing unit to be replaced, and the optimization to be repeated. In consequence, the mixer was not commercially explored. More recently, Utracki and coworkers (Nguyen and Utracki, 1995; Bourry et al., 1998) designed, tested and patented an extensional flow mixer, EFM.

Although the initial experimental results on extrusion through the EFM have been highly encouraging, the problem of understanding the mechanism leading to the successful operation of the device has not been resolved; optimization of the geometry and the processing

conditions remain heavily dependent on empiricism. Several geometrical and materials characteristics, which are known to affect the quality of mixing in the convergent–divergent flow, will be examined in this study. These factors usually determine the relative effect of shear or elongation on drop deformation, and affect both the dispersive and distributive mixing. Since drop deformation in a (confined or unconfined) medium represents a problem of the moving-boundary type, the boundary-element method (BEM) is ideally suited for the treatment of this problem.

While extensive work has been devoted to the modeling and simulation of drops deforming in an infinite fluid medium, relatively little work has been done in the case of a drop deforming in a confined domain. In both cases, most simulations were carried out using the BEM. The reader is referred to Rallison (1984) for a review. More recently, the BEM has been extended to include the motion of a drop in the vicinity of a plane wall (Pozrikidis, 1990; Ascoli et al., 1990), and a deformable interface (Yiantsios and Davis, 1990). The deformation of drops in confined flow was analyzed inside a circular straight tube (Martinez and Udell, 1990; Pozrikidis, 1992), and in a tube with constriction (Tsai and Miksis, 1994). These studies, however, examined only axisymmetric motion. The drop deformation was therefore confined along the axis of the channel.

The present paper is part of a series of studies on the application of the BEM to problems in mixing, polymer processing and interfacial phenomena (Khayat et al., 1995, 1997, 1998; Boury et al., 1998). The study focuses on the planar deformation of a drop in a convergent–divergent channel for drops moving along and off the channel axis. The suspending fluid and drop can be either Newtonian or viscoelastic. The mathematical foundation for the method in the case of a Newtonian system (drop and suspending fluid) was already established elsewhere (Khayat et al., 1997). The general boundary-element formulation for a linear viscoelastic fluid developed by Khayat et al. (1998) will be applied to examine viscoelastic drop/matrix systems.

The inherent transient nature of the flow process and the presence of a moving interface between drop and suspending fluid make the simulation challenging because of the nonlinearities involved in the description of the interface (Floryan and Rasmussen, 1989). The challenge becomes even greater if both inertia and non-Newtonian effects are accounted for (Bird et al., 1987; Khayat and Garcia-Rejon, 1992; Mao and Khayat, 1995). Nonlinear effects, such as those stemming from fluid elasticity, fluid inertia and shear thinning, are difficult to account for in a boundary-element approach despite the advent of recent techniques to handle nonlinear and transient problems (Wrobel, 1987; Nowak, 1995; Neves and Brebbia, 1991; Frayce and Khayat, 1996).

The boundary integral equations for viscoelastic fluids that are used in the current study are derived and solved in the time domain. This approach is unlike many existing BEM formulations for linear viscoelastic problems, which are carried out in the frequency domain. The derivation of the boundary integral equation is based on the Laplace transform of the flow variables. The association of the integral transform of the viscoelastic solution with that corresponding to the Newtonian flow problem is similar to the correspondence principle for linear viscoelastic solids or the elastico-viscoelastic analogy (Christensen, 1982). The proposed procedure involves replacing the viscosity by the appropriate form in the transformed equations, and reinterpreting the transformed flow variables as transformed viscoelastic field variables. The transformed equations are solved, and the solution is inverted, leading to the

evolution of the flow field in the time domain. In the present formulation, however, the inversion is avoided, and the boundary integral equations are obtained in the time domain. A time marching scheme is then implemented to determine the evolution of the drop/matrix interface (Khayat et al., 1997, 1998).

2. Problem formulation

In this section, a boundary integral equation is developed for a Maxwell fluid to determine the deformation of a drop in a confined medium. Further details on the formulation and assessment of the accuracy of the proposed approach, as well as other applications are discussed elsewhere (Khayat et al., 1997, 1998).

2.1. Governing equations

Consider a drop of viscosity η_d and relaxation time λ_d, moving under the influence of a suspending fluid of viscosity η_s and relaxation time λ_s. At any instant, the drop occupies a region $\Omega_d(t)$ and is neutrally buoyant, so the effects of gravity and any external body forces are neglected. The suspending fluid occupies the outer region, $\Omega_s(t)$, and is driven by an imposed pressure gradient. The regions $\Omega_s(t)$ and $\Omega_d(t)$ are assumed to be separated at all times by a moving interface, $\Gamma_i(t)$. Thus, situations where the drop comes in contact with the boundary of the channel, Γ_c, or where the drop breaks up into smaller droplets are excluded. The region $\Omega_s(t)$ is always bounded by $\Gamma_i(t)$ and Γ_c. Both the drop and the suspending fluid are viscous and incompressible. The fluids of interest are typical molten polymers of high viscosity subjected to small strain rates during processing. Thus, only low-Reynolds-number flow, typically characterized by small velocities, small length scales and/or high viscosity, will be considered. In this limit, the inertia terms in the momentum equation are negligible, and the two-phase system is in a state of creeping motion. The conservation of mass and momentum equations in each region may be written as:

$$\nabla \cdot \mathbf{u}_\alpha(\mathbf{x},t) = 0 \quad \nabla \cdot \boldsymbol{\sigma}_\alpha(\mathbf{x},t) = \mathbf{0} \quad \boldsymbol{x} \in \Omega_\alpha(t) \tag{1}$$

The subscript $\alpha = d$ and s, corresponding to a variable in the drop and suspending fluid region, respectively. Here ∇ is the gradient operator, $\mathbf{x}$ is the position vector, $\mathbf{u}_\alpha(\mathbf{x}, t)$ is the velocity vector, and $\boldsymbol{\sigma}_\alpha(\mathbf{x}, t)$ is the total stress tensor. In terms of the hydrostatic pressure $p_\alpha(\mathbf{x}, t)$ and excess stress tensor $\boldsymbol{\tau}_\alpha(\mathbf{x}, t)$, $\boldsymbol{\sigma}_\alpha(\mathbf{x}, t) = -p_\alpha(\mathbf{x}, t)\mathbf{I} + \boldsymbol{\tau}_\alpha(\mathbf{x}, t)$, where $\mathbf{I}$ is the unit tensor. All dependent and independent variables have been made dimensionless using a reference length, L, for spatial coordinates, a typical flow velocity, U, for the velocity components, L/U for time, and $\eta_s U/L$ for stress and pressure. These reference parameters will be defined later when a given flow geometry is examined.

The fluids are assumed to obey the linear viscoelastic constitutive equation of the Maxwell type. In dimensionless form,

$$We_d \frac{\partial \boldsymbol{\tau}_d(\mathbf{x},t)}{\partial t} + \boldsymbol{\tau}_d(\mathbf{x},t) = R_\eta[\nabla \mathbf{u}_d(\mathbf{x},t) + (\nabla \mathbf{u}_d(\mathbf{x},t))^t] \quad \mathbf{x} \in \Omega_d(t) \tag{2a}$$

$$We_s \frac{\partial \boldsymbol{\tau}_s(\mathbf{x},t)}{\partial t} + \boldsymbol{\tau}_s(\mathbf{x},t) = \nabla \mathbf{u}_s(\mathbf{x},t) + (\nabla \mathbf{u}_s(\mathbf{x},t))^t \quad \mathbf{x} \in \Omega_s(t) \tag{2b}$$

Three dimensionless groups have been introduced in the current problem, namely the two Weissenberg numbers, We_α, in $\Omega_\alpha(t)$, and the drop-to-suspending-fluid viscosity ratio, R_η:

$$We_\alpha = \frac{\lambda_\alpha U}{L} \quad R_\eta = \frac{\eta_d}{\eta_s} \tag{3}$$

It is clear from the governing equations (1) and (2) that, unlike the viscosity ratio, the ratio of the relaxation times does not constitute a similarity parameter. There are two other similarity groups, namely, the aspect ratio of the channel and the capillary number. This latter will be defined later when the influence of interfacial tension is examined.

The boundary conditions are the same as those for a Newtonian system. These conditions consist of the dynamic and kinematic conditions at the interface, and no-slip and no-penetration conditions at the channel wall. Poiseuille flow is assumed to hold at the entrance and exit of the channel. Both the drop and the suspending fluid are assumed to be at a state of rest initially. For further details, the reader is referred to Khayat et al. (1997).

2.2. Boundary integral equations for drop deformation

The integral equation for general viscoelastic flow was derived elsewhere for one-phase flow (Khayat et al., 1998). Only a summary of the derivation is given here. The first step in deriving the integral equations consists of taking the Laplace transform of the conservation equations (1), finding that the transformation conserves the same form of the initial continuity and momentum equations in the Laplace domain. An expression is thus obtained from Eq. (2) for the transformed excess stress in terms of the transformed rate-of-strain tensor, which is mathematically equivalent to Newton's law of viscosity. The formulation is then pursued as if the problem corresponded to the flow of a Newtonian fluid in the frequency domain.

The integral equation in the time domain is obtained by taking the inverse Laplace transform of the integral equation in the frequency domain. The derivation of the resulting equations in the $\Omega_\alpha(t) \cup \Gamma_\alpha(t)$ domain is carried out similarly to single-fluid flow (Khayat et al., 1998), leading to:

$$\begin{aligned} &\int_{\Gamma_c \cup \Gamma_i(t)} \mathbf{n}(\mathbf{y},t) \cdot \left[We_s \frac{\partial \boldsymbol{\sigma}_s(\mathbf{y},t)}{\partial t} + \boldsymbol{\sigma}_s(\mathbf{y},t) \right] \cdot \mathbf{J}(\mathbf{x} \mid \mathbf{y}) \, d\Gamma_y \\ &\quad - \int_{\Gamma_c \cup \Gamma_i(t)} \mathbf{n}(\mathbf{y},t) \cdot \mathbf{u}_s(\mathbf{y},t) \cdot \mathbf{K}(\mathbf{x} \mid \mathbf{y}) \, d\Gamma_y = c_s(\mathbf{x},t)\mathbf{u}_s(\mathbf{x},t) \quad \mathbf{x} \in \Omega_s(t) \cup \Gamma_c \cup \Gamma_i(t) \end{aligned} \tag{4a}$$

$$\begin{aligned} &\int_{\Gamma_i(t)} \frac{\mathbf{n}(\mathbf{y},t)}{R_\eta} \cdot \left[We_d \frac{\partial \boldsymbol{\sigma}_d(\mathbf{y},t)}{\partial t} + \boldsymbol{\sigma}_d(\mathbf{y},t) \right] \cdot \mathbf{J}(\mathbf{x} \mid \mathbf{y}) \, d\Gamma_y - \int_{\Gamma_i(t)} \mathbf{n}(\mathbf{y},t) \cdot \mathbf{u}_d(\mathbf{y},t) \cdot \mathbf{K}(\mathbf{x} \mid \mathbf{y}) \, d\Gamma_y \\ &\quad = c_d(\mathbf{x},t)\mathbf{u}_d(\mathbf{x},t) \quad \mathbf{x} \in \Omega_d(t) \cup \Gamma_i(t) \end{aligned} \tag{4b}$$

The term $c_\alpha(\mathbf{x}, t)$ takes the same meaning as for Stokes flow for $\mathbf{x} \in \Omega_\alpha(t) \cup \Gamma_\alpha(t)$, and it depends on time since the domain occupied by the fluid changes with time. It is obvious that, for the present problem, $\Omega_\alpha(t) = \Omega_d(t)$ and $\Gamma_\alpha(t) = \Gamma_i(t)$ for the fluid occupying the drop region, and $\Omega_\alpha(t) = \Omega_s(t)$ and $\Gamma_\alpha(t) = \Gamma_s(t) \equiv \Gamma_i(t) \cup \Gamma_c$ for the suspending fluid. Here **J** and **K** are second and third rank tenors, which are also the same for Stokes flow (Khayat et al., 1997).

The first step in solving Eqs. (4a) and (4b) consists of introducing a finite-difference approximation in time to handle the stress derivatives (Khayat et al., 1998). Two coupled integral equations that govern the velocity at the interface and the traction at the channel wall are then obtained similarly to those corresponding to the Newtonian system (Khayat et al., 1997) with extra source (boundary) integrals involving the stress at the previous time step.

3. Influence of shear and elongation in convergent-divergent flow

In this section, the planar deformation of droplets subject to the flow of the suspending fluid inside a confining channel is examined. The accuracy of the method was previously assessed elsewhere (Khayat et al., 1995, 1997) and will not be pursued here. Although the flow in channels of arbitrary geometry may easily be handled by the current formulation, the computations are confined to a symmetrical, hyperbolic convergent-divergent channel. The following influential geometric and materials characteristics of the two-phase system will be investigated in this section:

- Drop size relative to the channel dimension(s).
- Drop-to-suspending-fluid viscosity ratio.
- Initial drop distance from the channel axis.
- Initial horizontal drop position relative to the channel entrance.
- Interfacial tension at the drop interface.
- Relaxation times of drop and suspending fluid.

The size of the drop and its initial position relative to the axis of the channel are particularly important. These factors determine the relative dominance of shear and elongation effect from the suspending fluid on drop deformation. Thus, if the drop is large relative to the channel opening, or positioned away from the channel axis, then the influence of shear flow, originating from the channel wall, is significant. On the other hand, if the drop size is relatively small, or the drop moves close to the channel axis, then the elongational flow dominates.

The deformation of a large and low-viscosity drop in the convergent-divergent channel is typically illustrated in Fig. 1. The reference length, L, is taken as the half-length of the channel. The dimensionless length of the channel is then equal to 2, the entrance and exit widths are each equal to 1.4, and the neck width is equal to 0.14. Poiseuille flow is imposed at the entrance and exit of the channel, and the maximum velocity is taken as the reference velocity, U. Throughout this section, the channel width-to-length ratio will be fixed to 0.7. For these and all subsequent calculations in this geometry, the number of boundary elements is fixed equal to 96 along the channel boundary, and 48 along the drop/fluid interface. Both fluids in Fig. 1 are assumed to be Newtonian ($We_d = We_s = 0$) interfacial tension effects are

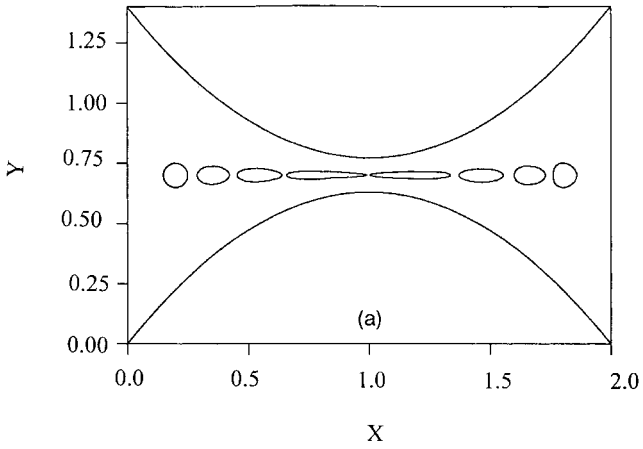

Fig. 1. Newtonian drop of initial diameter $D_0 = 0.1$ and viscosity ratio $R_\eta = 2$ flowing through a hyperbolic convergent–divergent flow channel ($We_s = We_d = Ca^{-1} = 0$). The figure shows the channel geometry and the drop deformation along the channel axis.

neglected ($Ca^{-1} = 0$). The viscosity ratio $R_\eta = 2$ and the initial (dimensionless) drop diameter $D_0 = 0.1$. The evolution of the drop shape is shown at various positions along the channel axis. The drop stretches in the converging flow region, reaches maximum elongation in the neck region, and recovers its initial (circular) shape as it nears the exit. This symmetric recovery is not always possible as will be seen next.

3.1. Influence of drop size

The influence of shear and elongation on drop deformation is first investigated by examining the influence of the initial drop size D_0 and viscosity ratio R_η. The relative deformation, $\alpha(t)$, of the drop is taken as the relative change of the current perimeter of the drop, $P(t)$, at time t, with respect to the initial perimeter, P_0, i.e. $\alpha(t) = [P(t) - P_0]/P_0$. This definition of the deformation is reasonable given the convoluted shape that the drop may assume during deformation. The evolution of α may be plotted against either time or position along the channel axis. The time representation, however, is found to be more revealing of the deformation dynamics.

Two viscosity ratios are examined for three initial sizes of a drop deforming along the channel axis. For a relatively low viscosity ratio, $R_\eta = 2$, the results are shown in Fig. 2 for three values of the initial drop diameter $D_0 = 0.02$, 0.06 and 0.1. The top of the figure displays the change in drop shape with position along the channel axis, while the lower part displays the evolution of the corresponding relative deformation as a function of time. The results reflect an essentially similar shape evolution for the three drops; there is practically no effect of the initial drop size on the subsequent deformation for a relatively small value of the viscosity ratio, $R_\eta \leqslant 2$. Typically, the deformation reaches a maximum in the neck region, and decreases as the drop recovers its initial shape (there is symmetry in deformation). One may conclude that, for relatively small viscosity ratio, and for a relatively small drop initially placed on the

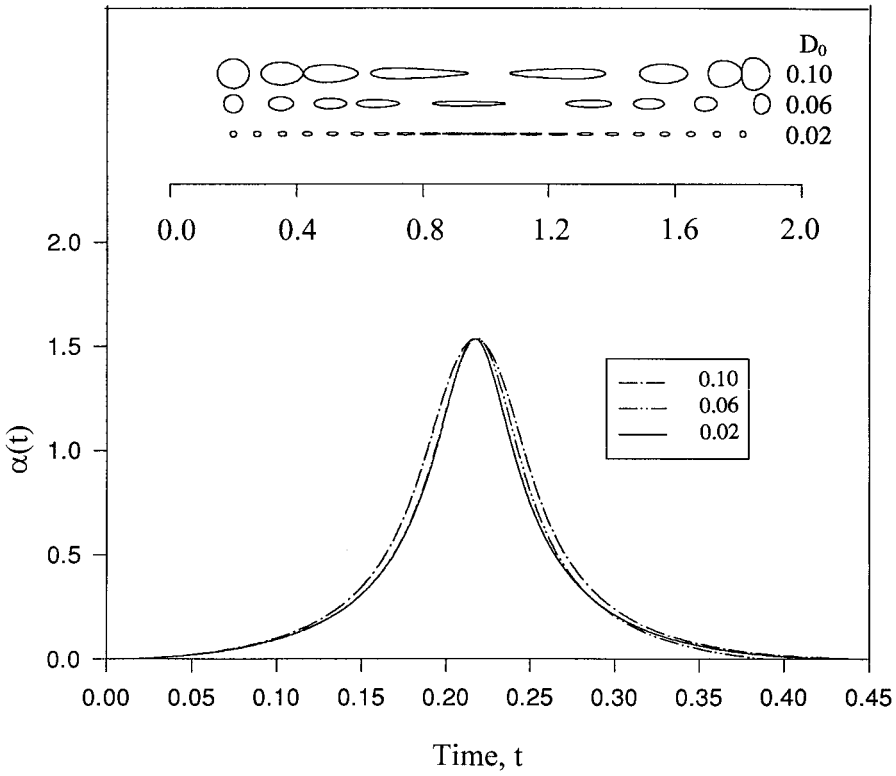

Fig. 2. Influence of the initial drop size on deformation for $0.02 \leqslant D_0 \leqslant 0.1$ and $R_\eta = 2$ ($We_s = We_d = Ca^{-1} = 0$). The evolution of the drop shape along the channel axis is shown in the upper part of the figure, and that of the deformation is shown in the lower part. Note the symmetry in deformation with respect to neck region.

channel axis, the relative deformation is essentially independent of the drop size, as it is due mainly to elongation; shear effects are negligible. Even for large drops, the relatively low drop viscosity allows the drop to stretch significantly enough in the neck region for elongation effects to remain predominant. This argument may be taken to the limit of an air bubble ($R_\eta \to 0$); the deformation of large and small bubbles is essentially the same!

For a relatively high viscosity ratio, the situation is different. As the viscosity ratio further increases, the deformation becomes progressively more difficult, and the drop behaves like a solid. The evolution of drop shape and corresponding relative deformation for $R_\eta = 10$ is depicted in Fig. 3. In contrast to the situation illustrated in Fig. 2, here the drops do not recover their initial circular shape in the exit region. This is particularly evident for the larger drops. Furthermore, as the drops exit from the neck region, their rear end flattens. As evident from the magnitude of the relative deformation, $\alpha(t)$, more viscous drops elongate less. The α-curves also indicate that larger drops undergo higher deformation and show a loss of shape recovery (symmetry). This lack of symmetry is caused by the low elongation in the neck region and the shear effects that affect the outer region of the drop. Obviously, the shear effects are greater for the larger drop—this was already evident in the non-circularity of $D_0 = 0.1$ drop in Fig. 2 as the drop nears the exit. Furthermore, the results indicate that the maximum relative

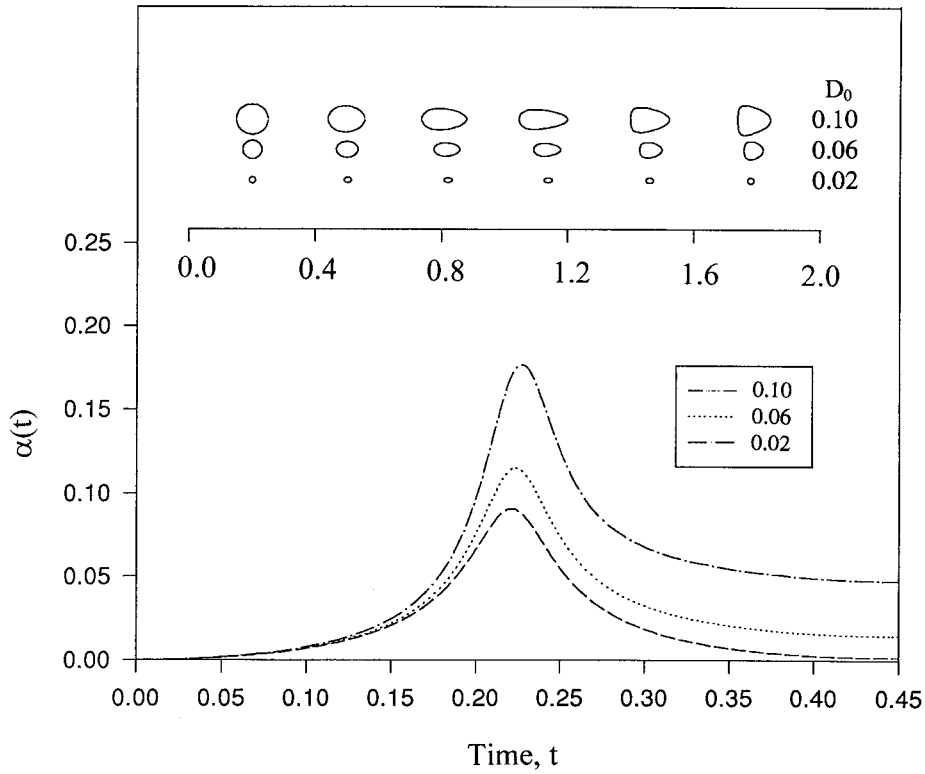

Fig. 3. Influence of the initial drop diameter on deformation for $0.02 \leqslant D_0 \leqslant 0.1$ and $R_\eta = 10$ ($We_s = We_d = Ca^{-1} = 0$). The evolution of the drop shape along the channel axis is shown in the upper part of the figure, and that of the deformation is shown in the lower part. Symmetry is observed only for the smallest drop. Note the loss in symmetry for all three drops.

deformation occurs earlier for the smaller drops, slightly ahead of the maximum convergence. Thus, while small drops moving along the channel axis tend to experience mainly extensional flow regardless of the viscosity ratio, larger drops become significantly subjected to shearing, especially those of moderate or large viscosity ratios.

3.2. Influence of viscosity ratio

The influence of the viscosity ratio was extensively explored previously (Khayat et al., 1997). Some of the earliest work on the theory of the small deformation at low Reynolds numbers was carried out by Taylor (1932, 1934), who considered three-dimensional (3D) drop deformation in elongational flow at constant strain rate, $\dot{\varepsilon}$. The deformation was assumed to be small enough for the shape of the deformed drop to remain close to spherical. Defining the droplet deformation as $\kappa_d(t) = D(t)/D_0$, where $D(t)$ is the current droplet major axis and D_0 is the initial drop diameter, the evolution of droplet deformation with time was predicted as:

$$\kappa_d(t) = 1 + \frac{5}{2R_\eta + 3}\dot{\varepsilon}t \tag{5}$$

At small strains, the local elongation imposed by the suspending fluid is simply:

$$\kappa(t) = e^{\dot{\varepsilon}t} \cong 1 + \dot{\varepsilon}t \tag{6}$$

leading to the following relation

$$\frac{\kappa_d(t) - 1}{\kappa(t) - 1} = \frac{5}{2R_\eta + 3} \tag{7}$$

Palierne (1990) showed that the Eq. (7) also holds for an arbitrary time-dependent flow provided that the deformation remains small.

In the present case, the rate of elongation of the suspending fluid is estimated by placing a drop of equal viscosity ($R_\eta = 1$) in the neck region. The ratio of the relative deformation of a drop of arbitrary viscosity ratio to a drop of relative viscosity equal to one is then extrapolated to the initial time, $t = 0$. Fig. 4 shows the behavior of this limit as function of the viscosity ratio. The diameter of the drops considered is too small ($D_0 = 0.02$) for shear effects from the walls to be significant. The results shown in Fig. 4 are in qualitative agreement with the behavior predicted by Taylor (1932, 1934) and Palierne (1990) as expressed in Eq. (7). The deformation ratio is equal to 1 for $R_\eta = 1$. When $R_\eta > 1$, the ratio asymptotically decreases to zero as $R_\eta \to \infty$. On the other hand, when $R_\eta \to 0$, the ratio of the deformations increases asymptotically to 5/3, not to about 2 as predicted by Eq. (7). This discrepancy, although small, is due to the fact that the present results are based on a confined and not infinite ambient flow.

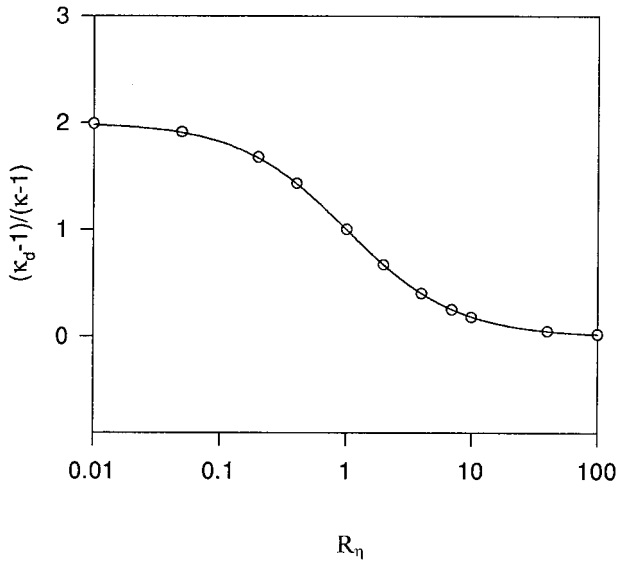

Fig. 4. Influence of the viscosity ratio on the deformation of a relatively small drop of initial diameter $D_0 = 0.02$ and the viscosity ratio $R_\eta \in [0.01, 100]$ ($We_s = We_d = Ca^{-1} = 0$). The ratio of the drop deformation to the deformation of the fluid matrix is plotted against R_η.

In this case, the flow cannot be purely elongational. In addition, the present formulation is two-dimensional whereas Eq. (7) is based on a 3D formulation.

3.3. Influence of initial position

In this section, the effect of the drop initial position will be examined. The drop may be initially located either off the channel axis (vertical shift), or on the channel axis at different distances from the neck center (horizontal shift). Thus, if the drop is initially positioned far from the channel axis, then the influence of shear flow in the vicinity of the channel wall should be significant.

The effect of initial distance from the channel axis is examined for a drop of initial diameter $D_0 = 0.02$ and two viscosity ratios: $R_\eta = 4$ and 10. The results are presented in Figs. 5 and 6, respectively. To assess the influence of the initial position, the evolution was monitored for three drops, nos 1, 2 and 3. Drop 1 is initially placed on the axis (at $y = 0.7$), drop 2 is initially located 0.2 off the axis ($y = 0.5$), and drop 3 is initially located 0.3 off the axis ($y = 0.40$). As the results in Fig. 5 indicate, the initial displacement of the drop influences both the rate and the magnitude of drop deformation. Thus, drop 2 deforms similarly to drop 1 but at a slower pace. As it reaches the neck region and approaches the channel axis, it stretches slightly more than drop 1. Furthermore, the figure also indicates that in the

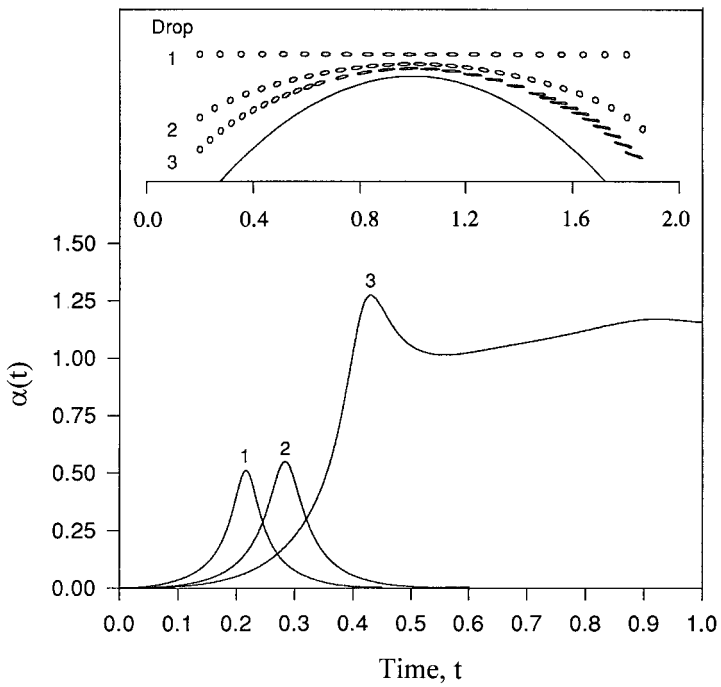

Fig. 5. Influence of the initial position for drops 1, 2 and 3, located off the channel axis by distances: 0, 0.2 and 0.3, respectively. The size of the drops is $D_0 = 0.02$ and $R_\eta = 4$ ($We_s = We_d = Ca^{-1} = 0$). The evolution of the drop shape inside the channel is shown in the upper part of the figure, and that of the deformation is shown in the lower part.

convergent part of the channel, drop 2 tends to be swept away from near the channel wall toward the channel axis. As the drop comes out of the neck region, it is swept back into the region near the wall, where (see α versus t dependence), similarly to drop 1, it recovers its initial shape. For drop 3, the deformation is still slower and larger than that of drop 2. In the divergent zone, the drop begins to recover some of its circular shape but eventually stretches again as it heads towards the exit. At this point, in contrast to drops 1 and 2, the drop remains significantly stretched and never recovers its initial shape. The influence of shearing is clearly important. The maximum deformations shown in Fig. 5 varied from 50% (drop 1), to 55% (drop 2), and to 125% (drop 3). It should be noted that the residence time within the channel of drop 3 is 2.22 times longer than that of drop 1.

The calculations that lead to the results shown in Fig. 5 were repeated for $R_\eta = 10$, and the results are shown in Fig. 6. Drop 1 moves along the channel axis, and it is included again for reference. Its deformation is symmetric with respect to the neck of the channel. Initially, drop 2 deforms similarly to drop 1, but at a rate roughly twice smaller than that of drop 1. In contrast to the behavior shown in Fig. 5 where the maximum in α increases as the drop is displaced farther from the axis, here the maximum decreases from 9% for drop 1 to about 5% for drop 2. The reason for this decrease is the rotation of the drop. The drop compression within the convergent part of the channel prohibits the stretching before the expected

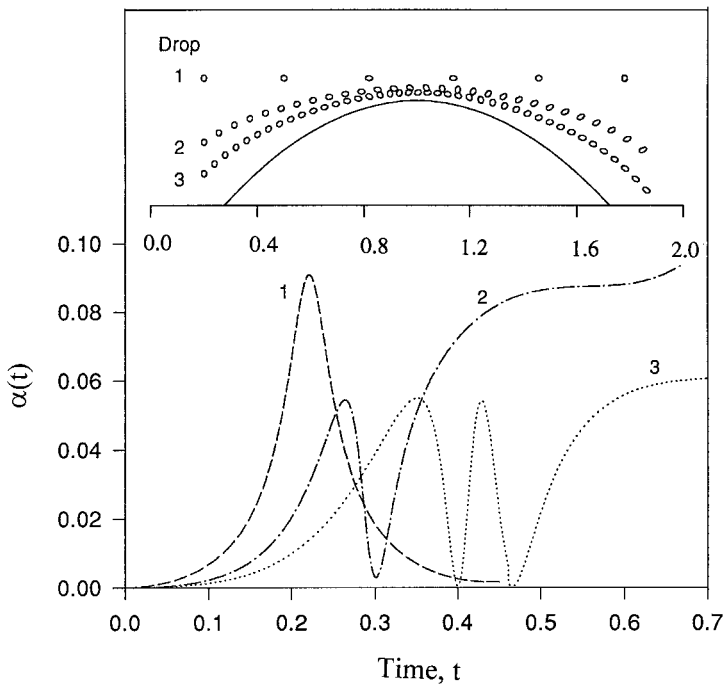

Fig. 6. Influence of the initial position for drops 1, 2 and 3, located off the channel axis by distances: 0, 0.2 and 0.3, respectively. Diameter of the drop is $D_0 = 0.02$ and $R_\eta = 10$ ($We_s = We_d = Ca^{-1} = 0$). The evolution of the drop shape inside the channel is shown in the upper part of the figure, and that of the deformation is shown in the lower part.

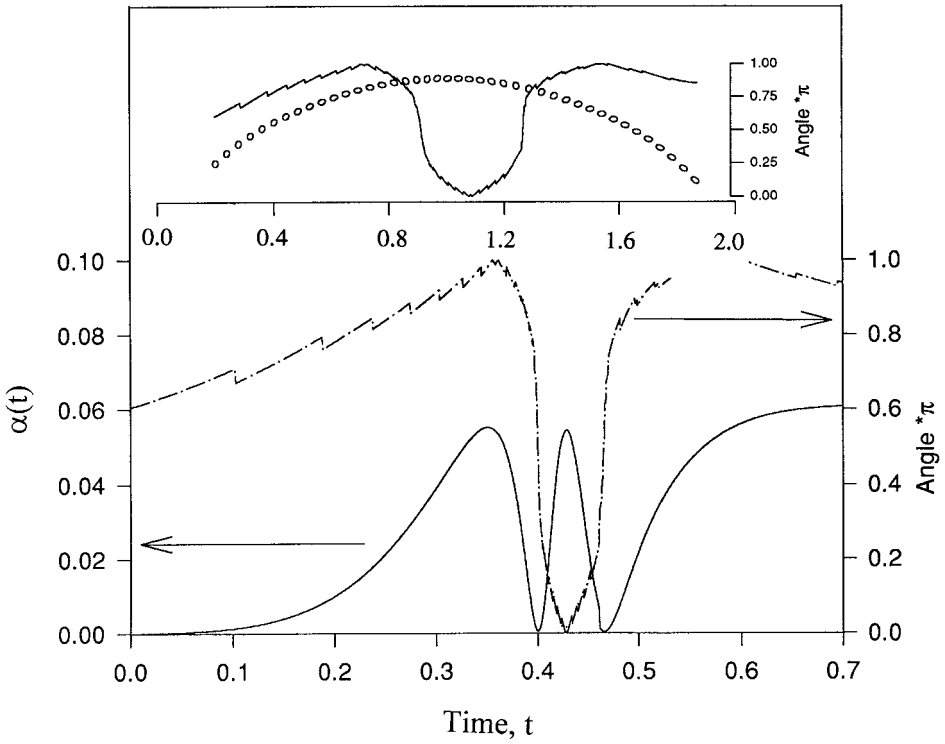

Fig. 7. Orientation of drop 3 (from Fig. 6) located 0.3 off the channel axis, having diameter $D_0=0.02$ and $R_\eta=10$ ($We_s=We_d=Ca^{-1}=0$). Evolution of the relative deformation, $\alpha(t)=[P(t)-P_0]/P_0$, as well as of the angle, $*\pi$, that the drop major axis makes with horizontal is plotted versus time in the lower part.

maximum deformation could occur at the neck. However, as the rotation slows down in the divergent part of the channel, the drop becomes subjected to further extension.

The shear flow component for drop 3 is greater than that for drop 2 as Fig. 6 indicates. The shear effect leads to the occurrence of a rotation of the slightly elongated drop. The rotation causes the drop to repeatedly stretch and compress as it flows through the channel. In this case, the maximum deformation reaches only about 6%. Similarly to drop 2, drop 3 is also more stretched in the divergent part of the channel, where the rotation rate slows down. Thus, for relatively large viscosity ratios, shearing has a minor influence on the drop deformation, its main effect is to generate the rotation of slightly deformed particles.

The orientation angle, β, of drop 3 (between its major axis and the channel axis) with respect to time and position is shown in Fig. 7. For the sake of completeness, the relative deformation from Fig. 6 is also included. The initial orientation angle $\beta=0.6\pi$ is taken to coincide with the orientation that the drop assumed a right position after the first increment in time. The drop appears to orient itself along the (local) tangent to the channel wall. As it moves away from the channel entrance, the angle increases along with the relative deformation until the drop becomes parallel to the channel axis, $\beta=\pi$, reaching the first maximum in deformation. Next, there is a sharp drop in the orientation angle, $\beta\rightarrow 0$. The change of orientation generates the

compressive force that at first eliminates the initial elongation, $\alpha \to 0$, then compresses the drop, thus causing the deformation to locally increase ($\alpha \to 0.05$). As the drop comes from the neck region, again it orients itself parallel to the channel axis, which causes a sharp increase in relative deformation. The drop appears to deform further from this point onwards undergoing relatively pure extension as the angle of orientation remains constant.

Additional insights on the role of shear and elongation are obtained by examining the influence of the viscosity ratio on the same drop size and location. In Fig. 8, the deformation of drop 3 ($D_0 = 0.2$, vertically displaced by 0.3; see Fig. 5) is shown for the range of $R_\eta \in [4,10]$. The figure illustrates the overall decrease in deformation as the drop viscosity increases. There is a significant shift in the first maximum to the left, indicating that, as the drop viscosity increases, the drop tends to reach maximum deformation earlier. The curves in Fig. 8 should be compared with those in Fig. 4. The reason is related to the period of rotation of the drop, t_p. Theory predicts that $t_p = 2\pi(p + 1/p)/\dot{\gamma}$, where p is the aspect ratio and $\dot{\gamma}$ is the shear rate (Goldsmith and Mason, 1967). Thus, the fastest rate of rotation is expected for spheres, the slowest for long fibers or flat discs. As the viscosity increases, the drop deformation decreases, $p \to 1$, and the period of rotation increases. This translates, on the one hand, in compression of the drops to occur sooner, and, on the other, in a larger number of extrema.

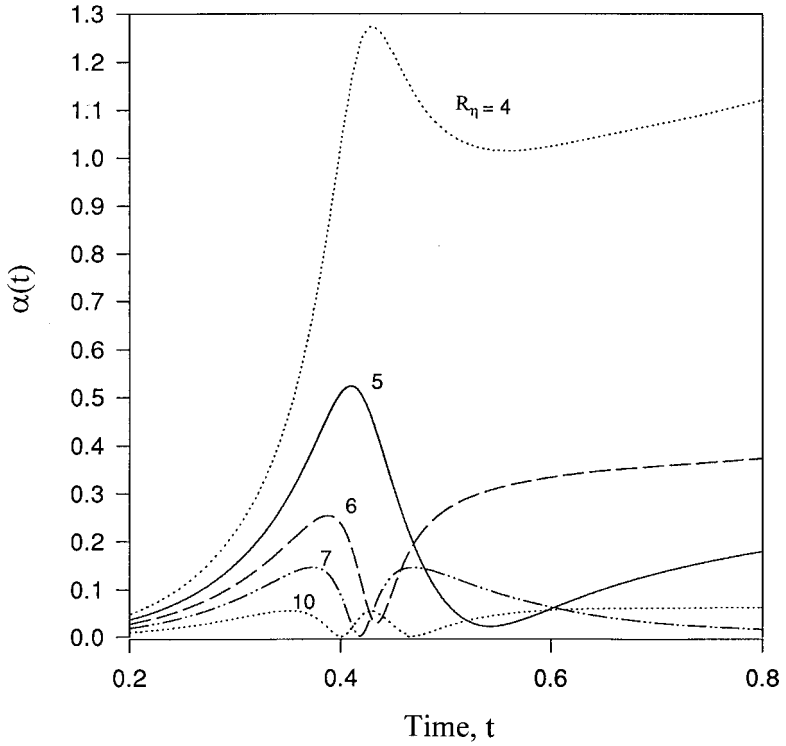

Fig. 8. Influence of the viscosity ratio, $R_\eta \in [4, 10]$, on the deformation of drop 3 from (from Fig. 7) located 30 mm off the channel axis, having diameter $D_0 = 0.02$ and $R_\eta = 10$ ($We_s = We_d = Ca^{-1} = 0$).

Next, consider the influence of the initial horizontal shift on the deformation for relatively large drops flowing on the channel axis, having viscosity ratio $R_\eta = 4$ and initial diameter $D_0 = 0.1$. The results are depicted in Fig. 9. One of the drops is initially located near the channel entrance (labeled as drop 1 in the following text) and is monitored as it deforms in the converging part of the channel. The second drop is initially located at the center of the channel neck (labeled as drop 2), and is monitored as it deforms in the divergent part of the channel. Fig. 9 displays the shape and the deformation, $\alpha(t)$ at various stages of flow for $D_0 = 0.1$. Note that the position scale is the same for drops 1 and 2. The two drops cover essentially the same distance but deform differently, one in the converging part and the other in the diverging part. As before, drop 1 tends to deform slowly near the entrance and stretches rapidly as it reaches the neck region. Drop 2 deforms significantly more. In this case, $\alpha(t)$ tends to be roughly linear with t. In contrast to drop 1, drop 2 deforms typically like a drop subjected to shear flow. Drop 2 is more strongly affected by the shear flow in the neck region. In consequence, it reaches a relative deformation three times larger than that of drop 1.

3.4. Influence of interfacial tension

So far the effect of interfacial tension has been neglected. The capillary number, Ca, is expressed in terms of the maximum shear rate, U/H, in the neck region of the suspending fluid

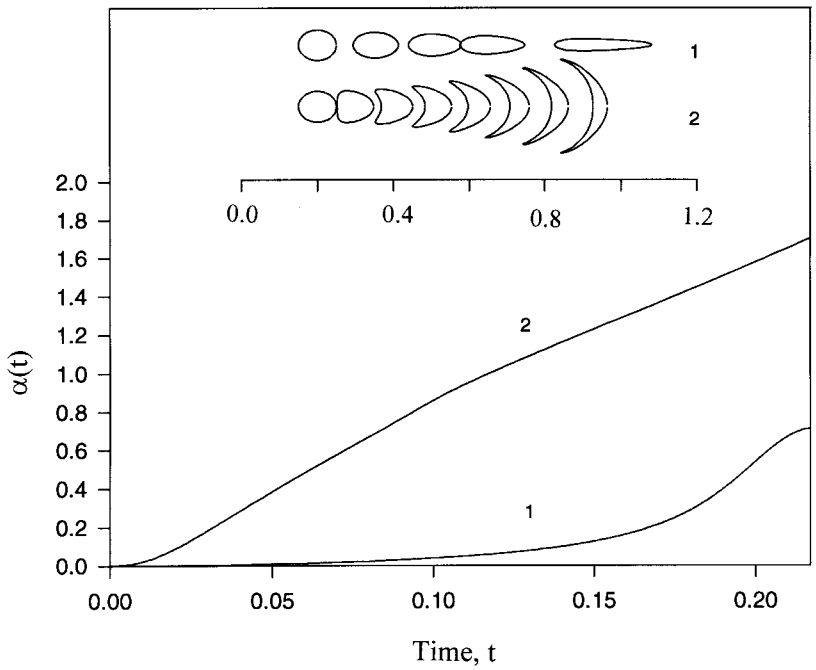

Fig. 9. Influence of the initial position on drop deformation. The initial drop diameter is $D_0 = 10$ mm and viscosity ratio $R_\eta = 4$ ($We_s = We_d = Ca^{-1} = 0$). The drop is located on and is moving along the channel axis. Thus, the relative deformation, $\alpha(t)$, is plotted against time for the drop located initially near the channel entrance (drop 1), and in the neck (drop 2).

(where H is neck width), η_s, D_0, and the interfacial tension ν. Thus, $Ca = D_0 U \eta_s / \nu H$. The calculations show that for a small drop ($D_0 = 0.02$), the evolution of deformation is essentially independent qualitatively from interfacial tension, at least for the range $Ca^{-1} \in [0, 25)$ and $R_\eta \in [4,10]$. The drop tends to recover its initial shape. The time, τ, of recovery is shorter as Ca^{-1} increases. Thus, as expected, interfacial tension tends to reduce the drop deformation in the convergence and accelerates recovery of the drop in the divergence. The relaxation time, τ, depends strongly on Ca. This dependence is illustrated in Fig. 10 as τ is plotted against Ca^{-1} for $R_\eta = 4$ and 10. For both viscosity ratios, τ decreases monotonically with Ca^{-1}, with a sharper drop for the smaller relative viscosity.

3.5. Influence of fluid elasticity

The influence of fluid elasticity is now examined in the absence of interfacial tension ($Ca^{-1} = 0$) for several values of the Weissenberg numbers We_d and We_s. So consider first the deformation of a small drop of initial diameter $D_0 = 0.02$ moving along the channel axis. The viscosity ratio $R_\eta = 5$. The evolution of the relative deformation is shown in Fig. 11. The case of a Newtonian drop moving in a Newtonian matrix ($We_s = We_d = 0$) is included for reference. The figure indicates that a Newtonian drop ($We_d = 0$) deforms less as the elasticity of the suspending fluid increases. This decrease in deformation is evident from the curves $We_s \in [0,$

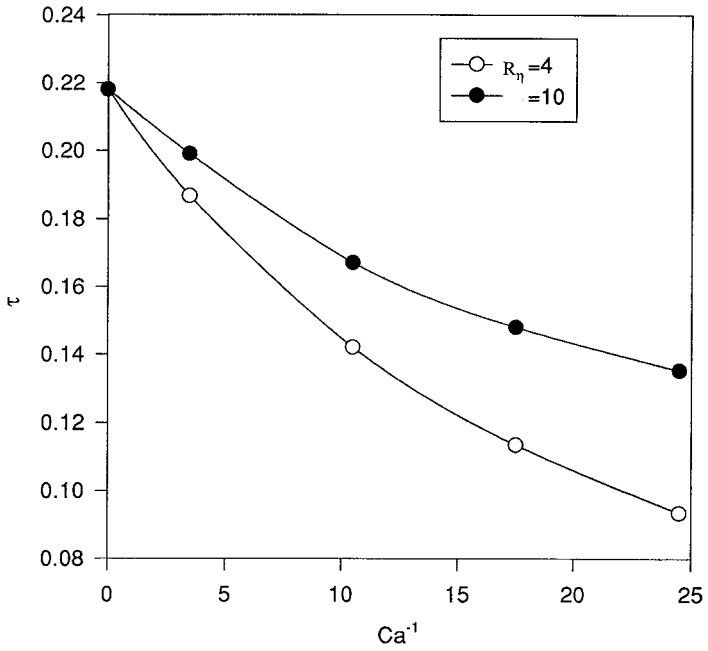

Fig. 10. Dependence of the time, τ, the drop takes to relax from the maximum deformation α to zero as function of Ca^{-1}. The initial drop diameter is $D_0 = 0.02$, and the relative viscosity $R_\eta = 4$ (lower curve) and 10 (upper curve) ($We_s = We_d = 0$).

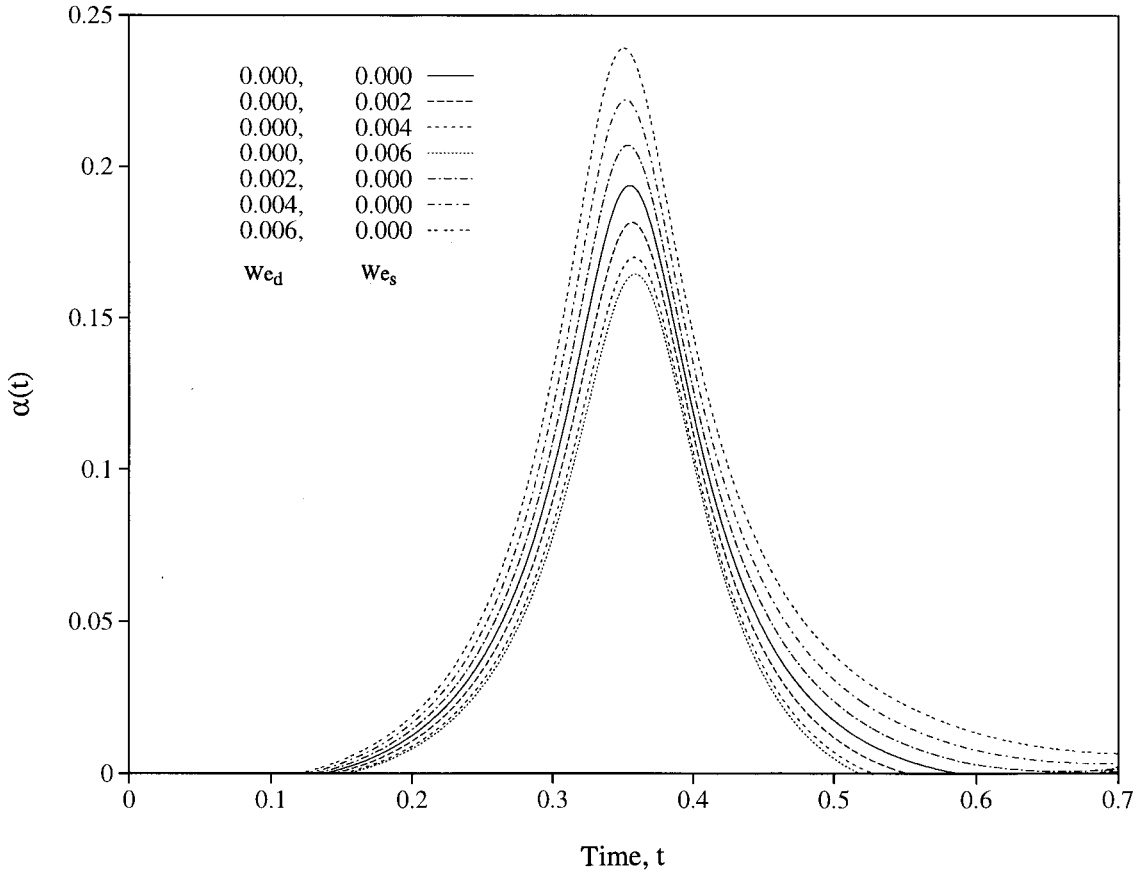

Fig. 11. Influence of fluid elasticity on drop deformation for a small drop ($D_0 = 0.02$, $R_\eta = 5$ and $Ca^{-1} = 0$) moving along the channel axis. The curves correspond to the evolution of deformation for a viscoelastic drop in a Newtonian matrix, with $We_s = 0$ and $We_d \in [0,\ 6 \times 10^{-3}]$, and a Newtonian drop in a viscoelastic matrix with $We_s \in [0,\ 6 \times 10^{-3}]$ and $We_d = 0$. Note that the curve $We_s = We_d = 0$ corresponds to a Newtonian system.

6×10^{-3}]. In this case, deformation is symmetric as the drop recovers its circular shape near the exit. For a viscoelastic drop moving in a Newtonian suspending fluid, the deformation increases as We_d increases (see the curves corresponding to $We_s = 0$, $We_d \in [0,\ 6 \times 10^{-3}]$). In this case, symmetry is lost gradually as the drop fluid elasticity increases.

The fact that fluid elasticity tends to enhance deformation is somewhat surprising, as one expects elasticity to oppose deformation (one can easily picture the stretching of an elastic band to be much more difficult than that of a liquid band!). However, the results shown in Fig. 11 are based on a *linear* (Maxwell) constitutive model, which describes the true fluid behavior under conditions of small deformation rates only. To illustrate the role of elasticity more clearly, consider the deformation of a drop of relaxation time λ and viscosity η in purely elongation flow in the x direction. The ambient fluid exerts a stress τ_{xx} inducing a rate of strain $\partial u_x/\partial x$ over the drop domain that is given by:

$$\frac{\partial u_x}{\partial x} = \frac{1}{\eta}\left(\lambda\frac{\partial \tau_{xx}}{\partial t} + \tau_{xx}\right) = \frac{1}{\eta}\left[\tau_{xx}^k + \frac{\lambda}{\Delta t}(\tau_{xx}^k - \tau_{xx}^{k-1})\right] \tag{8}$$

where the transient term has been approximated by finite difference. For a Newtonian fluid, the deformation is equal to τ_{xx}^k/η, which shows that drops with smaller viscosity tend to undergo higher deformation. The second equality in Eq. (8) indicates that, for $\lambda \neq 0$, there is an additional contribution to $\tau_{xx}^k - \tau_{xx}^{k-1}$ if the stress increases with time. Thus, in situations where the drop is initially stress free, the stress (magnitude) can only grow in time, leading to the additional contribution. This is indeed the present case, as the stress is assumed to be initially equal to zero. This assumption may not be realistic, since at $t = 0$ the drop immediately adjusts to, and starts moving with the surrounding flow.

The results in Fig. 11 are in agreement with the findings of Bousfield et al. (1986), who considered the breakup of viscoelastic filaments. They followed the evolution of an imposed disturbance on a filament of dilute polymer solution obeying the Oldroyd-B constitutive equation (Bird et al., 1987) using a transient finite-element solution and a one-dimensional thin filament approximation. They found that the disturbance initially grows much more rapidly on the viscoelastic filament (see Fig. 8 in the paper by Bousfield et al., 1986).

It is worth noting that, in the absence of interfacial tension, the deformation is independent of the fluid elasticity when the relaxation time of the drop is the same as that of the suspending fluid ($We_d = We_s$). In fact, deformation is the same as that corresponding to a Newtonian system. Of course, the value of the actual tractions at the channel wall and at the interface changes with the level of elasticity, but the kinematics (drop deformation) of the flow remains the same. The absence of dependence of $\alpha(t)$ on $We_d = We_s$ becomes obvious once the tractions on both sides of the drop/matrix interface are eliminated between Eqs. (4a) and (4b). When Eq. (4b) is multiplied by R_η and subtracted from Eq. (4a), one ends up with the difference in tractions and that of their time derivatives on either sides of $\Gamma_i(t)$. In the absence of interfacial tension these two differences are zero, which leads to an integral equation for the velocity at the interface independent of We_s and We_d (see Khayat et al., 1997, 1998).

Finally, another issue worth exploring is the effect of the *ratio* of relaxation times or We_d/We_s. As mentioned earlier, unlike R_η, the ratio of the relaxation times is not a similarity group. It is thus important to see what effect it has on drop deformation as We_d and We_s are varied while keeping the ratio constant. The effect can be depicted from Fig. 12 for a relatively large drop ($D_0 = 0.1$) moving along the channel axis and $R_\eta = 10$ ($Ca^{-1} = 0$), when the drop-to-matrix relaxation-time ratio is kept equal to 2, $We_d \in [0.004, 0.048]$ and $We_s \in [0.002, 0.024]$. The top part of the figure displays the evolution of the drops for each case, and the corresponding evolution of drop deformation is shown in the lower part of the figure. The figure indicates that deformation is essentially the same in the convergent part as the drop typically elongates like a relatively small viscosity (Newtonian) drop. In the lower We_d range, a drop typically deforms like a high-viscosity drop by recuperating some of its circular shape as it nears the exit. In this case, the drop deforms little but shear effects are somewhat significant. As We_d increases further deformation increases. The drop remains significantly deformed in the divergent zone and elongation effects remain predominant. It is thus obvious that the ratio of the relaxation times is not a similarity parameter.

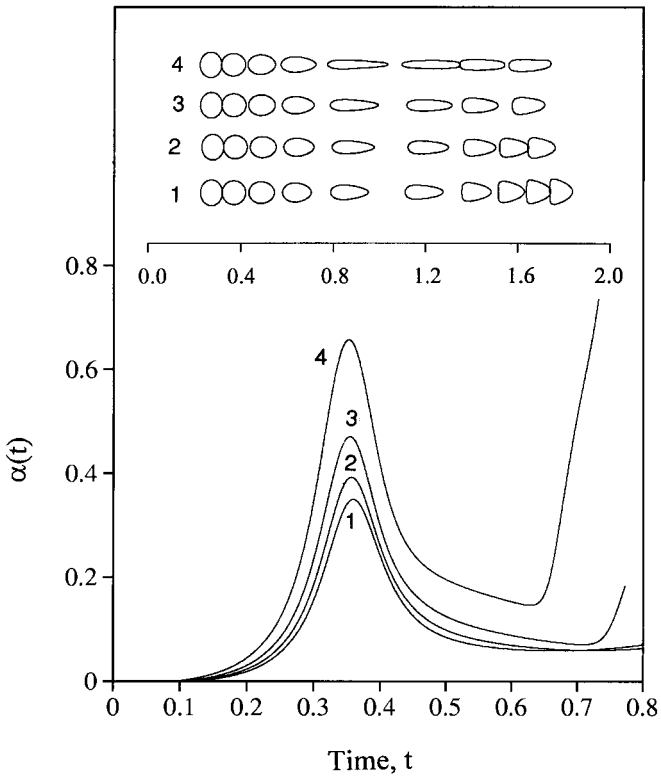

Fig. 12. Influence of the fluid elasticity for large drops of relaxation time equal twice that of matrix fluid ($We_d/We_s=2$) moving along the channel axis. The initial diameter of the drops is $D_0=0.1$ and $R_\eta=10$ ($Ca^{-1}=0$). The evolution of the drop shape along the channel axis is shown in the upper part of the figure, and that of the deformation is shown in the lower part. Drops 1–4 correspond, to ($We_s=0.004$, $We_d=0.002$), (0.012, 0.006), (0.024, 0.012) and (0.048, 0.024), respectively.

4. Experiment and the slit-flow model

The purpose of the present experimental study is to examine the drop deformability in convergent slit flow and compare it to predictions of the boundary-element method. Both Newtonian and non-Newtonian fluids are studied with $R_\eta > 1$.

4.1. Experimental setup

The experiments were performed in a convergent-divergent slit cell, shown in Fig. 13. The cell is symmetrical, with 30 mm long convergent and divergent parts (60° convergence and divergence) connected with two parallel plates either 79 or 130 mm long. The slit gap between these plates was kept constant at $H = 3.2$ mm. In the figure, the variable, $0 < r$ (mm) < 33, is

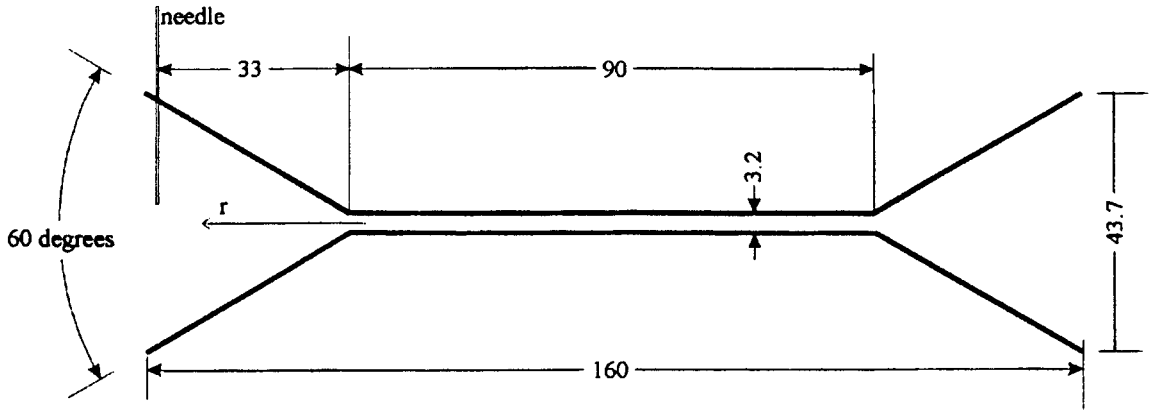

Fig. 13. The convergent–divergent slit cell geometry.

also defined—it is the distance from the origin of the convergence toward the entrance to the cell. The matrix fluid was circulated through the cell by means of compressed air. A manual valve was used to control the flow. First, a drop of the dispersed liquid was injected into the stationary matrix using a Hamilton syringe. The injected fluid was removed from the needle by inducing the matrix fluid to flow at low rate for a brief period. After the flow was stopped, a spherical drop was formed near the needle tip.

The syringe needle can be inserted into any horizontal position across the conical entry zone, i.e. it is possible to inject the drop directly to the axial flow (where the extensional effects are at maximum), or off-axis where the drops are subjected to combined shear and elongation. The drop deformation studies were performed at relatively low flow rates of the matrix, controlled by pre-selected pressure gradient. The shape of the drops was monitored and recorded using a Sony CCD video camera. Some sequences were scanned to determine the kinetics of drop deformation and/or recovery. In these cases, the position, velocity, and shear rate were computed from the initial position to the time needed to reach the end of the cell.

4.2. Model fluids

For the Newtonian matrix fluids, polydimethylsiloxane, PDMS, and corn syrup, were used. The drops were formed using one of the following liquids:

1. Newtonian polymeric fluids.
2. Viscoelastic 'Boger' fluid (based on high molecular weight polystyrene, PS, dissolved in a solution of medium molecular weight PS in DOP).
3. Viscoelastic solution of polyacrylamide, PAM, in water.

Values of the shear viscosities were determined as: $\eta_s = 6$–60 Pas for the matrices; and $\eta_d = 13.5$–600 Pas for the drops, see Table 1.

Table 1
Fluid systems used in experiment

Matrix fluid	Drop fluid	System	η_s (Pas)	η_d (Pas)	R_η	ν (mN/m)[a]
PDMS[b]	PB	N9	60	530	8.83	3.65
PDMS	PB	N3	60	180	3	3.65
PDMS	1% PAM in H_2O (solution l1)	VE10	60	600	10	12.98
Corn syrup	0.075% HMW PS in PS-DOP 28/72 (Boger PS)	VE2.2	6.0	13.5	2.25	5.87

[a] The interfacial tension was computed from Girifalco and Good (1957).
[b] The following abbreviations are used in the text: PDMS, polydimethylsiloxane; PB, polybutene-1; PAM, polyacrylamide; PS, polystyrene; HMW PS, high molecular weight polystyrene; DOP, di(ethylhexyl)phthalate.

4.3. Drop breakup

From the experiments, it is found that the Newtonian and Boger fluid drops do not break up even when elongated four times the initial diameter. However, the drops made of PAM solution do break. The breakup is observed at the extremity of the drop elongated in the convergent region and entering the parallel plate section of the profile (see Fig. 14). At this position, the tail of the drop is stretched, then breaks up into small droplets. A linear relation between the time-to-break and the maximum velocity is found. The critical drop diameter for the breakup decreases as the flow rate increases.

It is worth noting that by contrast to the Boger fluid (whose shear viscosity is nearly constant), the solution of PAM is pseudoplastic. Experiments are still being conducted to examine whether the observed breakup is due to the pseudoplasticity or to such factors as the slit gap to drop diameter (h/D_0) ratio.

5. Comparison between theory and experiment

Additional computational results based on the BEM are now presented. Comparison is made between theory and experiment wherever possible to further validate the proposed formulation and algorithm. Given the large ratio of the span to the height of the channel, the ambient flow may be assumed to be two-dimensional. However, in the presence of a drop, the drop deformation and the flow around the drop are three-dimensional. In this case a direct quantitative comparison between theory and experiment is meaningless. Nevertheless, a qualitative agreement between the two-dimensional theory and experiment is achieved upon comparison.

5.1. The basic flow

For a Newtonian matrix, the flow on the centerline of the convergence is purely extensional. Here, the centerline flow velocity, V, is inversely proportional to the axial distance from the convergence point, r, inside the slit: $V \cdot r = \text{constant}$, whereas the extensional flow rate is proportional to the square of the position, $\dot{\varepsilon} r^2 = \text{const.}$ (see Fig. 15). As defined in Fig. 13, r is

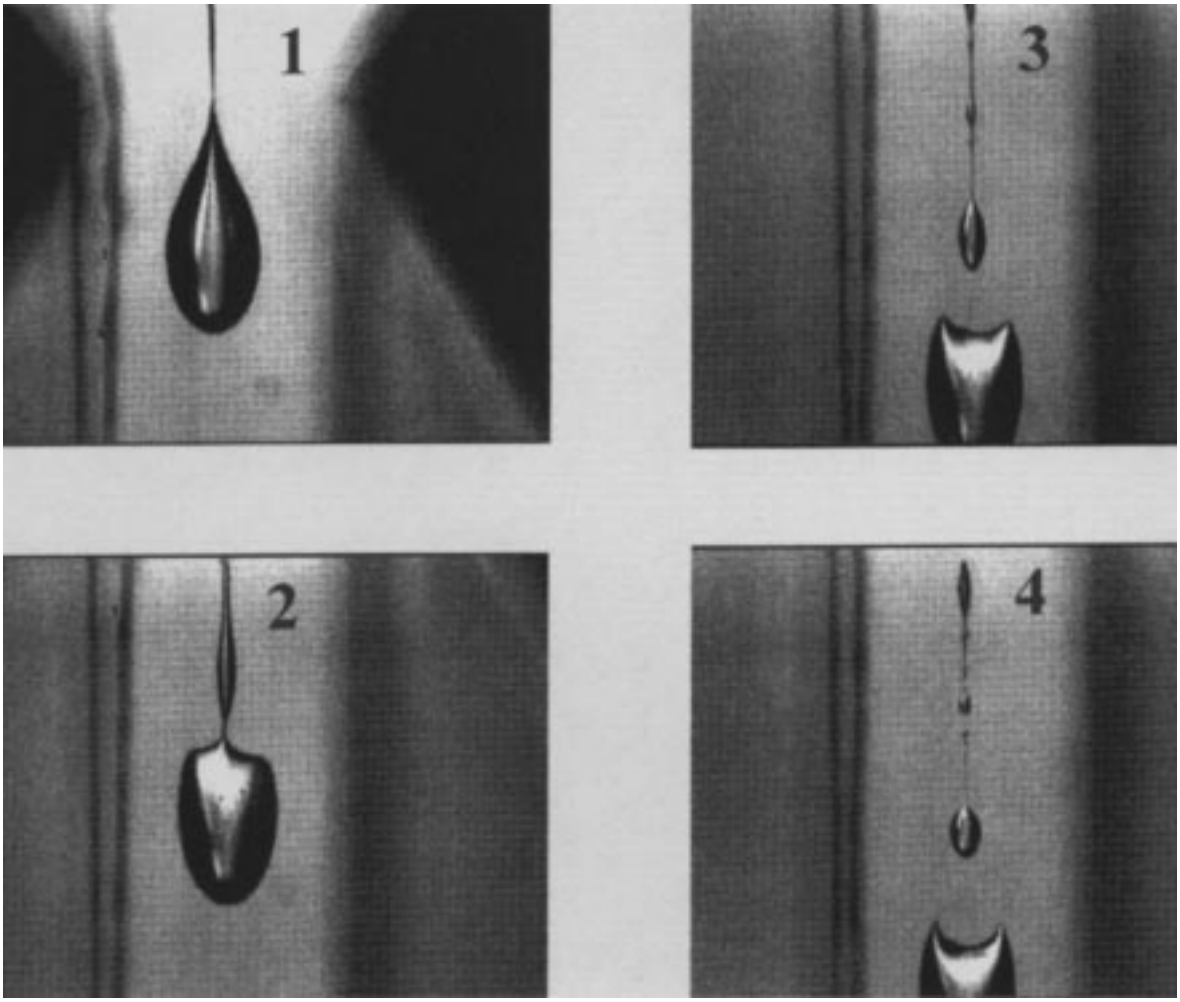

Fig. 14. Drop breakup at the slit entrance. The time sequence is indicated: left up, left down, right up, and right down.

the axial position coordinate, with $r = 0$ coinciding with the origin of the convergence just after the entrance to slit. Fig. 15 shows the velocity profile based on the BEM with no drop in the channel. Good agreement is obtained between theoretical and experimental results. This agreement shows that: (i) the basic BEM implementation is accurate; and (ii) 3D effects are not significant as far as the ambient flow inside the channel flow is concerned.

5.2. Drop deformation during the flow

Experiments were carried out using drop/matrix pairs with the viscosity ratio: $R_\eta = 3$, 8.8, and 10, at different flow rates. The deformability, d, was determined from the recorded drop deformation in the convergent and the divergent parts of the cell. An example of the result is shown in Fig. 16 for PB/PDMS system with the viscosity ratio, $R_\eta = 8.8$ (black points). In the

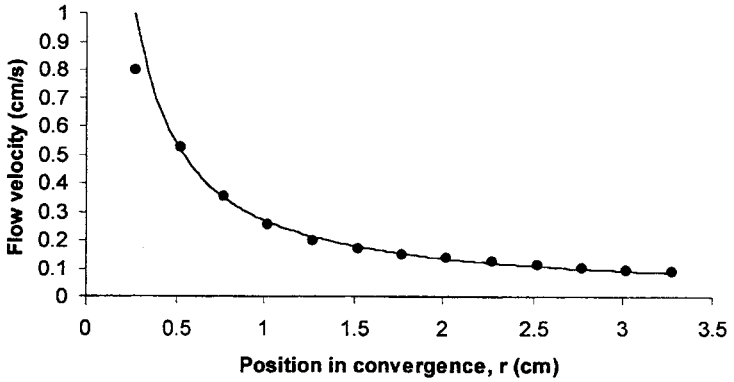

Fig. 15. The extensional flow velocity as a function of the position in the convergent part (r, from the slit position outward, see Fig. 13). Points are experimental, and the line shows the predicted hyperbolic dependence predicted by the BEM.

figure the data computed from the 2D BEM are also shown (open squares). Note that the position 3.3 cm corresponds to the entrance to the slit cell and zero the end of the convergence inside the slit. The 2D BEM prediction should be equated to 3D crossectional deformability of an infinitely long cylindrical drop flowing through the slit cell. As the data in Fig. 16 indicate, the BEM computations predict smaller drop deformability than that observed in 3D experiment. The comparison thus indicates that long drops (fibers) placed transversally to the flow tend to deform less than shorter drops with the same cross sectional area.

5.3. Influence of the initial position

The BEM is also used to simulate the drop deformation in the convergent-divergent flow of the slit cell used in the model experiments (the cell is shown in Fig. 13). In this case, the 2D computations are limited to the conical converging part, using Newtonian drops with $R_\eta = 2$, 3,

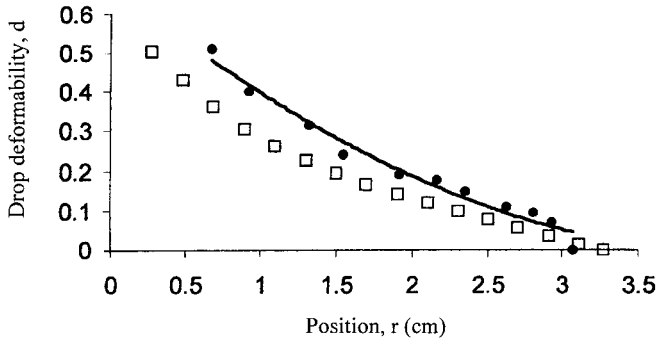

Fig. 16. Drop deformability, d, as a function of position in the convergent part of the cell, r. Full circles are experimental, obtained for the PB/PDMS system with $R_\eta = 8.8$. The line is a least-squares fit to the second order polynomial. The open squares were computed using the BEM.

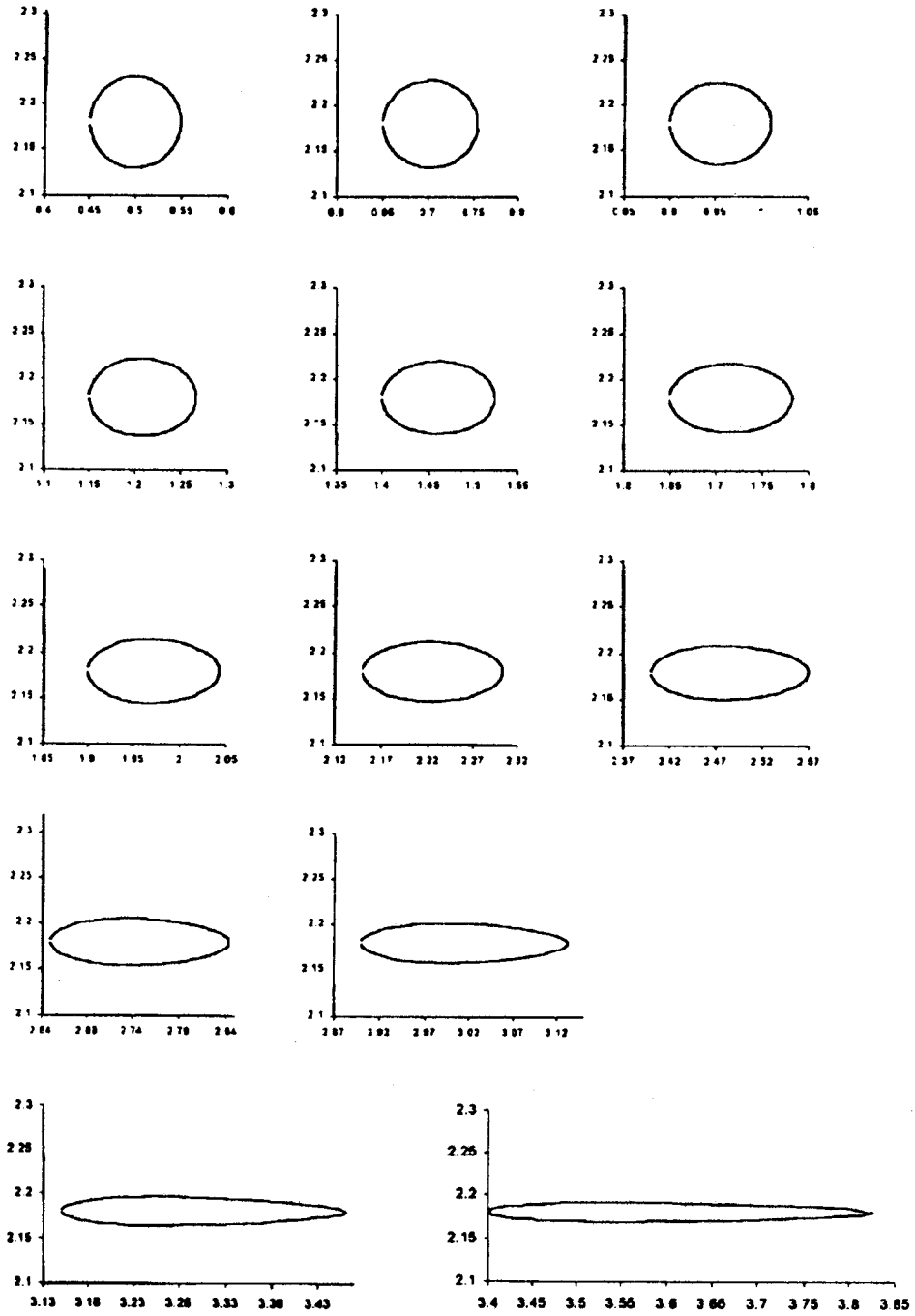

Fig. 17. Computed 2D deformation on the channel axis of a Newtonian drop as a function of its location inside the conical convergence. The initial drop diameter is $D_0 = 0.0125$, and its viscosity ratio: $R_\eta = 3$. The channel geometry is shown in Fig. 13.

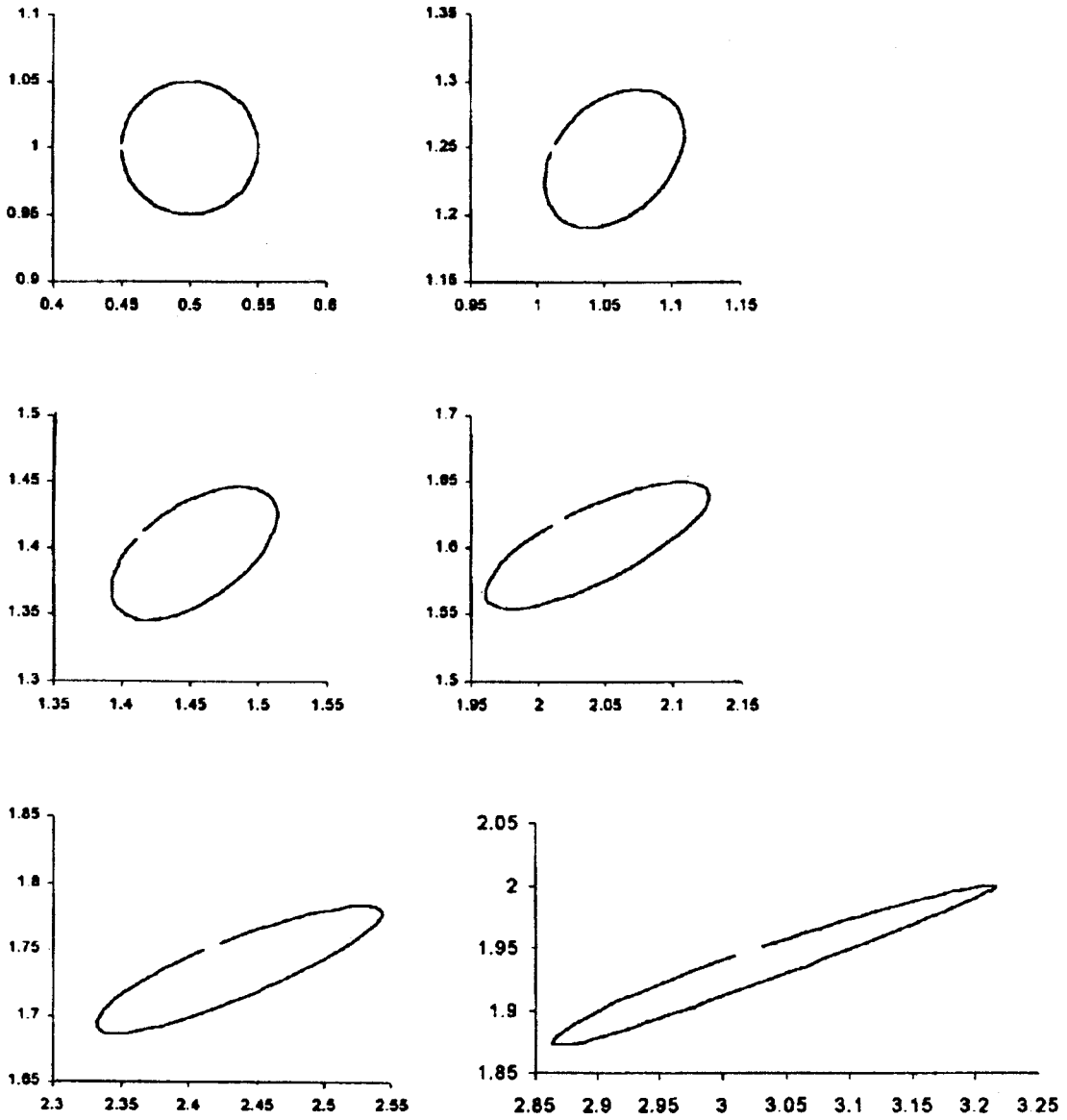

Fig. 18. Computed 2D deformation off the channel axis of a Newtonian drop as a function of its location inside the conical convergence. The initial drop diameter is $D_0 = 0.0125$, and its viscosity ratio: $R_\eta = 3$. The channel geometry is shown in Fig. 13.

8 and 10. Since the experiments were conducted with initially placing a drop either on or off the flow axis, the computations are carried out to simulate these two situations as well.

Examples of these computations are shown in Figs. 17 and 18 for drops moving on and off the axis, respectively. The initial drop diameter $D_0 = 0.0125$ and the viscosity ratio $R_\eta = 3$. The origin of the BEM grid coincides with the lower left angle of the cell shown in Fig. 13. Agreement between theory and experimental visualization is generally good. This becomes

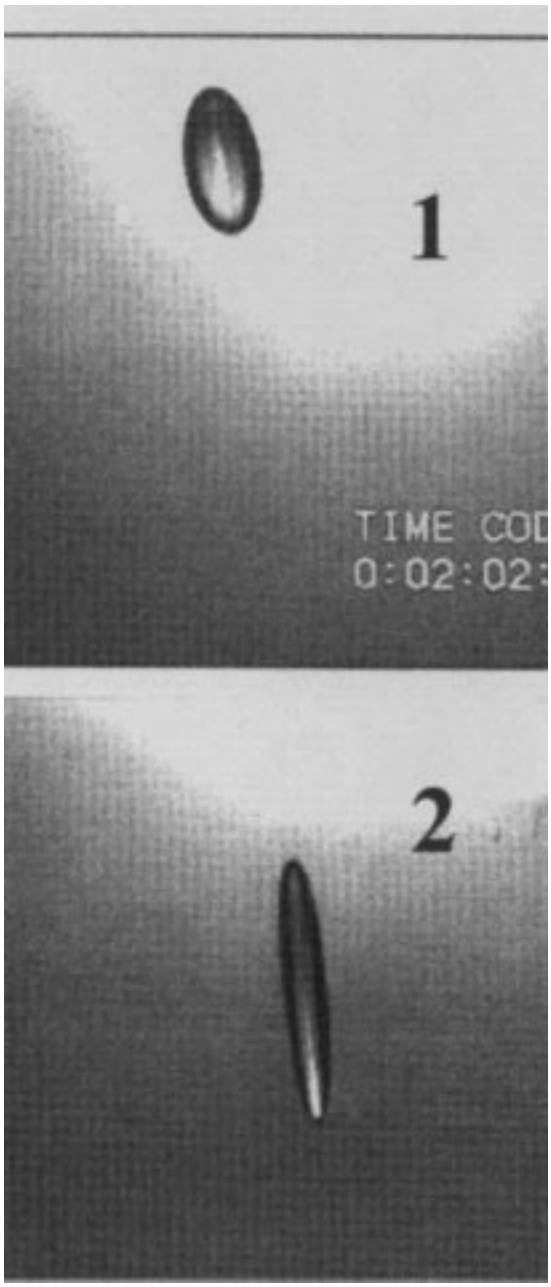

Fig. 19. Deformation of PB drop in PDMS matrix, $R_\eta = 3.0$. The initial drop diameter is about 0.0125. Compare these shapes with BEM results in Fig. 17, positions 1.4 and 3.0.

evident upon comparison between the evolution of the computed drop shape in Fig. 17 and the visualized shape in Fig. 19. Even a quantitative agreement is reached for the drop moving along the channel axis despite the limitations of the theory. This is confirmed upon comparison the drop shape at positions 1.4 (5th image) and 3.0 (11th image) in Fig. 18 with the observations presented in Fig. 19. Once again, agreement is not expected since the flow in reality becomes highly dimensional as the drop approaches the channel wall.

6. Conclusions

The influence of shear and elongation on drop deformation is investigated by examining the effects of flow geometry and material properties of the drop-matrix system of Newtonian and viscoelastic fluids. Such effects include the drop size, viscosity ratio, initial position of the drop relative to the channel axis (vertical shift), initial position relative to the neck center along the channel axis (horizontal shift), interfacial tension and fluid elasticity. Both theory and experiment are presented.

For a relatively low viscosity ratio, $R_\eta = 2$, the deformation of drops placed on the channel axis is independent of the initial drop diameter $D_0 = 0.02-0.1$. However, as R_η increases, the deformation decreases with decrease of D_0 and with increase of R_η. Furthermore, for the larger drops and higher R_η there is a loss of shape recovery (symmetry). The magnitude of the drop-to-matrix deformation in extensional flow (on the channel axis) is found to be in a qualitative agreement with small perturbation theory.

The initial vertical displacement of the drop relative to the channel axis influences the rate and magnitude of drop deformation. However, these effects are strongly altered by R_η. For $R_\eta \leqslant 4$, the shear flow increases the drop residence time in the channel, which in turn enhances the total deformation. On the other hand, for higher values of the viscosity ratio, the drops showed little deformation, tumbling along the channel, and being alternatively stretched or compressed.

During the convergent flow of two drops—one viscoelastic (Maxwellian) and the second Newtonian (both having the same viscosity ratio, R_η)—the former initially deforms more than the latter. Unlike the viscosity ratio, the relaxation-time ratio is not a similarity parameter in problem. Good agreement is obtained between the BEM 2D computations and experimental data for flow of immiscible liquids through a slit. The agreement is limited to drops with diameter significantly smaller than the slit gap, thus not affected by the wall effects.

References

Ascoli, E.P., Dandy, D.S., Leal, L.G., 1990. Boundary-driven motion of a deformable drop toward a planar wall at low Reynolds number. J. Fluid Mech. 213, 287.

Bird, R.B., Armstrong, R.C., Hassager, O., 1987. Dynamics of Polymeric Liquids, 2nd Ed., vol. 1. Wiley, New York.

Bourry, D., Godbille, F., Khayat, R.E., Luciani, A., Picot, J., Utracki, L.A., 1998 Extensional flow of polymeric dispersion, Polym. Eng. Sci. (in press).

Bousfield, D.W., Keunigs, R., Marrucci, G., Denn, M.M., 1986. Nonlinear analysis of the surface tension driven breakup of viscoelastic filaments. J. Non-Newtonian Fluid Mech. 21, 79.

Christensen, R.M., 1982. Theory of Viscoelasticity, 2nd ed. Pergamon Press, Oxford.
Elmendorp, J.J., 1986. A study on polymer blending microrheology. Ph.D. thesis, Delft University of Technology, The Netherlands.
Erwin, L., 1991. Principles of laminar fluid/fluid mixing. In: Rauwendaal, C. (Ed.), Mixing in Polymer Processing. Marcel Dekker, New York.
Floryan, J.M., Rasmussen, H., 1989. Numerical methods for viscous flows with moving boundaries. Appl. Mech. Rev. 42, 323.
Frayce, D., Khayat, R.E., 1996. A dual reciprocity boundary element approach to three-dimensional transient heat conduction as applied to materials processing. Numer. Heat Transfer A 29, 243.
Girifalco, L.A., Good, R.J., 1957. A theory for the estimation of surface and interfacial energies. I. Derivation and application to interfacial tension. J. Phys. Chem. 61, 904.
Goldsmith, H.L., Mason, S.G., 1967. In: Eirich, F.R. (Ed.), Rheology. Theory and Applications. Academic Press, London.
Grace, H.P., 1971. 3rd Engineering Foundation Research Conference on Mixing, Andover, NH, 9–14 August.
Han, C.D., 1981. Multiphase Flow in Polymer Processing. Academic Press, New York.
Khayat, R.E., Garcia-Rejon, A., 1992. Uniaxial and biaxial unsteady inflation of a viscoelastic material. J. Non-Newton. Fluid Mech. 43, 31.
Khayat, R.E., Derdouri, A., Hebert, L.P., 1995. A boundary-element approach to three-dimensional gas-assisted injection molding. J. Non-Newton. Fluid Mech. 57, 253.
Khayat, R.E., Luciani, A., Utracki, L.A., 1997. Boundary-element analysis of planar drop deformation in confined flow. Part I. Newtonian fluids. Engng Anal. Bound. Elem. 19, 279.
Khayat, R.E., Derdouri, A., Frayce, D., 1998 Boundary-element analysis of three dimensional transient mixing processes of Newtonian and viscoelastic fluids, Int. J. Num. Meth. Fluids 28, 815.
Mao, W., Khayat, R.E., 1995. Numerical simulation of transient planar flow of a viscoelastic materials with two moving free surfaces. Int. J. Num. Meth. Fluids 21, 1137.
Martinez, M.J., Udell, K.S., 1990. Axisymmetric creeping motion of drops through circular tubes. J. Fluid Mech. 210, 565.
Neves, A.C., Brebbia, C.A., 1991. The multiple reciprocity boundary element method for transforming domain integrals to the boundary. Int. J. Num. Meth. Engng. 31, 709.
Nguyen, X.Q., Utracki, L.A. 1995 US Patent, 5,451,106, 19 September (application 8 August 1984, to National Research Council of Canada, Ottawa).
Nowak, A.J., 1995. Application of the multiple reciprocity method for solving nonlinear problems. In: Wrobel, L.C., Brebbia, C.A., Nowak, A.J. (Eds.), Advanced Computational Methods in Heat Transfer II, Vol I: Conduction, Radiation and Phase Change. Computational Mechanics Publications, Southampton.
Palierne, J.F., 1990. Linear rheology of viscoelastic emulsions with interfacial tension. Rheol. Acta 29, 204.
Pozrikidis, C., 1990. The axisymmetric deformation of a red blood cell in a uniaxial straining Stokes flow. J. Fluid Mech. 216, 231.
Pozrikidis, C., 1992. Boundary Integral and Singularity Methods for Linearized Viscous Flow. Cambridge University Press, Cambridge.
Rallison, J.M., 1984. The deformation of small viscous drops and bubbles in shear flows. Ann. Rev. Fluid Mech. 16, 45.
Suzaka, Y. 1982 US Patent, 4,334,783, 15 June (application 21 December 1978, to Showa Denko, Kabushiki Kaisha, Oita, Japan).
Taylor, G.I., 1932. The viscosity of a fluid containing small drops of another. Proc. R. Soc. Lond. A 138, 41.
Taylor, G.I., 1934. The formulation of emulsions in definable fields of flow. Proc. R. Soc. Lond. A 146, 501.
Tsai, T.M., Miksis, M.J., 1994. Dynamics of a drop in a constricted capillary tube. J. Fluid Mech. 274, 197.
Utracki, L.A., Dumoulin, M.M., Toma, P., 1986. Melt rheology of high density polyethylene/polyamide-6 blends. Polym. Engng Sci. 26, 34.
Wrobel, L.C., 1987. The dual reciprocity boundary element formulation for nonlinear problems. Comput. Meth. Appl. Mech. Engng 65, 147.
Yiantsios, S.G., Davis, R.H., 1990. On the buoyancy-driven motion of a drop towards a rigid or deformable interface. J. Fluid Mech. 217, 547.